Potentiometric and SERS Detection of Single Nanoparticle Collision

Events on a Surface Functionalized Gold Nanoelectrode

Govinda Ghimire,¹ Popular Pandey,¹ Jing Guo,¹ Golam Sabbir Sarker,² Joongho Moon,^{2,3} Jin He^{1,3*}

Abstract

Single-entity electrochemistry is of fundamental importance and shows promise for ultrasensitive biosensing applications. Recently, we have demonstrated that various charged nanoparticles can be detected individually based on the non-redox open-circuit potential (OCP) changes induced by their collision events on a floating carbon nanoelectrode (CNE). Unlike the widely used amperometry approach, the potentiometric method provides the label-free detection of individual nanoscale entities without redox mediators in solution. However, the CNE lacks specificity for molecular recognition during the collision events because of the limited methods of surface functionalization for carbon surfaces. Herein, we used surface-functionalized gold nanoelectrode (GNE) to replace the CNE. The GNE modified with Raman reporter molecule also enabled surface-enhanced Raman spectroscopy (SERS) measurements. By using simultaneous time-resolved OCP and SERS measurements, both the OCP and SERS signals induced by the 'hit-n-run' type of gold nanoparticle (GNP) collision events can be better understood. Also, by introducing a zwitterionic molecule, we formed near 'stealth' surface and demonstrated that the non-specific adsorptions of GNPs to the surface of GNE have been suppressed, allowing continuous detection of hit-n-run events for over 30 minutes.

KEYWORDS: single-entity electrochemistry, electrochemical sensing, nanoelectrode, nano-impact, surface chemistry, SERS

¹Physics Department, Florida International University, Miami, Florida, 33199, USA

²Department of Chemistry and Biochemistry, Florida International University, Miami, Florida, 33199, USA

³Biomolecular Science Institute, Florida International University, Miami, Florida, 33199, USA

Introduction

The emerging field of single-entity electrochemistry (SEE) has made rapid progress in recent years because of the relatively low cost, little sample consumption, easy, fast, and ultrasensitive measurements of most SEE techniques.¹⁻⁷ Unlike the conventional ensemble average measurements, single-entity measurements can directly count and probe the behavior and properties of individual nanoscale entities, including nucleic acids, proteins, viruses, nanobubbles, and synthetic nanoparticles and nanostructures, with high throughput. These studies can improve our understanding of electrochemistry at the nanoscale and enable new applications in catalysis and electrochemical sensors. Among various single-entity techniques, extensive studies have been done on detecting the dynamic collision events of nano-entities (also called nano-impact) on ultrasmall electrodes using an amperometry approach.⁸⁻¹³ In this approach, the applied electrode potential induces faradaic current from the electrochemically active nano-entities or the redox mediators in the electrolyte during the nano-impact events. Relatively less studied, the redox process involved potentiometric approach has also been developed to detect nano-impact events. ¹⁴ In these studies, the collision-induced transient faradaic current or open-circuit potential (OCP) changes give information such as the size and concentration of various nanoentities being studied.

Recently, we have developed a non-redox-based potentiometric method to detect and analyze individual charged nanoscale entities by using the nano-impact induced transient potential changes of the floating carbon nanoelectrode (CNE). ^{15, 16} This simple label-free approach is mainly based on the charge sensing mechanism. ¹⁷ The collision event by a charged entity during the stochastic collision event can transiently disturb the electrostatic potential of the floating CNE, which can be sensitively detected. It is highly sensitive and even low molecular weight proteins can be detected individually. ¹⁸ In recent years, the potentiometric sensing methods for ensemble samples have experienced solid growth for biological sensing, especially in portable devices. ¹⁹ To enable the potentiometric nano-impact method for practical chemical and biological sensing applications, it is preferred to chemically functionalize the electrode surface as desired, which can improve the sensitivity and selectivity of this method. However, the reliable methods to chemically modify the carbon electrode surface are still very limited. ^{20, 21} In contrast, the gold electrode surface can be easily functionalized to form a self-assembled monolayer (SAM) with well-established methods. ²²

Herein, we demonstrated the use of functionalized gold nanoelectrode (GNE)²³ for the time-resolved potentiometric nano-impact measurements. To test the method, we used 40 nm size gold nanoparticles (GNPs) as the model nano-entities. The collision events of negatively charged GNPs on the surface of the floating GNE apex induce transient potential changes of the GNE, which has been measured by the connected high impedance potential differential amplifier. To verify these collision-induced transient potential changes, we also monitored the time-resolved surface-enhanced Raman spectroscopy (SERS) signals during the collisions of GNPs on the GNE modified with Raman reporter molecule biphenyl-4-thiol (BPT). Due to their extraordinary plasmonic property, the GNPs are often used to amplify the local light

field.^{24, 25} Here, the short stay of GNPs near the GNE surface can induce effective plasmonic resonance coupling and lead to the burst of light field confined inside the GNP-GNE nanogap. Indeed, some of the collision-induced transient potential dips were coupled with the transient significant increase in SERS intensity of surfacefunctionalized BPT molecules. Similar to the reported results of the amperometry experiments, ²⁶⁻²⁹ we found that the surface chemistry of GNE can greatly impact the behaviors of the GNPs collision. After modifying hydrophobic BPT molecules on the GNE surface, the negatively charged GNPs stayed for a much shorter time and further away from the GNE surface during the hit-n-run collision events. In an attempt to form a less hydrophobic and near 'stealth' surface for the GNE apex, we introduced the widely-used polyethylene glycol (PEG)³⁰ and zwitterionic molecules³¹ to mix with BPT molecules. With PEG, however, the GNE surface was found to be too hydrophilic and complex, leading to significantly increased GNPs adsorptions. Instead, with zwitterionic molecule N, N-Dimethyl-cysteamine-carboxybetaine (CBT),³² we found the non-specific adsorptions of GNPs on the GNE surface had been greatly suppressed, allowing continuous detection of 'hit-n-run' events of individual GNPs for over 30 minutes.

Experimental

Reagents and Materials. The BPT molecule (97%) was purchased from Sigma-Aldrich. The thiolated mPEG (MW-5000 purity >95%) was purchased from Nanocs. The CBT molecule was synthesized based on the previously reported protocol (see section S2, Supplemental Material).³² The 40 nm size citrate-capped GNPs were purchased from Ted Pella, *Inc.* All the aqueous solutions were prepared in deionized (DI) water from LabChem (ACS Reagent Grade, ASTM Type I).

GNE Fabrication and Functionalization. The GNEs were prepared from the 0.2 mm diameter gold wire (99.99% purity, EMS) following the electrochemical etching method reported previously.^{27, 33} The apex radius of the sharped GNEs was in the range of 200 - 400 nm. In the next step, the cleaned GNEs were insulated with high-density polyethylene (HDPE) layer so that only a small fraction of the apex surface was exposed (see Figure 1b). The exposed surface area of the GNE apex was approximately 1-4 μm², which was estimated by the diffusion-limited current in the steady-state cyclic voltammograms (CVs) (See Supplemental Material S1). To form a BPT SAM on the exposed GNE surface, the prepared GNEs were immersed in 10 mM of BPT solution in ethanol over 7 hours. To prepare the immersing solution for mixed SAM, the PEG (or CBT) aqueous solutions and BPT ethanol solution were mixed and the final solution contained 2 mM of PEG (or CBT) and 10 mM of BPT. The quality of the SAM was evaluated by the CVs (see section S1, Supplemental Material).

OCP Measurement. The potential of the floating NE was measured by using a homebuilt high impedance differential amplifier with a grounded Ag/AgCl wire electrode in the bath solution (10 mM PBS) as the quasi-reference electrode. The

amplifier's gain was kept at 1 and its bandwidth was higher than 25 kHz. The sampling rate was 50 kHz for all the measurements. Here, we only recorded the signals within the first 30 min after introducing GNPs to the bath solution.

SERS Measurement. All SERS measurements were conducted using a homebuilt Raman setup based on a Nikon Ti-U inverted optical microscope. The GNE was mounted near the liquid cell with its apex immersed in the solution (see Figure 1a). The 632.8 nm He-Ne laser beam was focused on the GNE apex using a 40x objective lens from the bottom. The typical radius of the laser spot on the apex is 2.5 μ m with a laser power of 0.9 mW, which gives an approximate power density of 45 μ W/ μ m². The scattered light was collected by the same objective lens. To detect the real-time changes in the SERS intensity, all the SERS trajectories were recorded with a time resolution of 50 ms per frame using the CCD camera (PIXIS 100B) eXcelon, Princeton Instrument).

Simultaneous SERS and OCP Measurement. Time-revolved SERS and potential measurements were synchronized by using the trigger signal generated by the CCD camera. The potential signals were recorded by using Axon Digidata 1440A (Molecular Devices *Inc.*, CA).

Simulation and Calculation Methods. The simulations of local electric field distribution and enhancement in the nanogap with different GNE-GNP distances were performed using the Finite-difference time-domain (FDTD) method (Ansys Lumerical's software) (see section S3, Supplemental Material).

The simulations of transient potential change (ΔV) of the floating GNEs with a GNP at different distances were conducted using the Finite element method (FEM) (COMSOL Multiphysics 5.2a software) and ΔV s were estimated using Poisson-Nernst-Planck (PNP) equations in chemical reaction engineering and AC/DC modules. More details about the simulation models and methods are given in section S5 of Supplemental Material.

The density-functional theory (DFT) calculations (Gaussian 09 package) were conducted to assign Raman peak positions for the BPT molecule. To better match the experimental conditions in SERS, we constructed the BPT-Au5 cluster complex structure (see section S4, Supplemental Material). Functional PW91/PW91 is used for the Raman spectra calculation. The basis set is 6-311G(d,p) for carbon, hydrogen, and sulfur atoms and is LANL2DZ for the gold atoms. A scale factor of 1.0056 is used for all vibrational bands. The calculated spectrum matches well with the experimental results.

Data Analysis. Data analysis was conducted by using pClamp software, and custom LabVIEW and MATLAB programs. The recorded potential time traces were filtered by using a 1 kHz low-pass Bessel filter. The plots were prepared in Origin Pro 2018.

Results and Discussion

As shown in Figure 1a, the individual GNP collision events on a GNE apex can be

monitored by the transient changes in the potential and simultaneously measured SERS signals. The HDPE insulated GNE with an exposed apex (see Figure 1b (i)) is connected to a high impedance differential amplifier for the OCP measurement. The laser beam is focused on the GNE apex for the SERS measurement, as shown in the optical microscope image of Figure 1b (i). The SEM image in Figure 1b (ii) shows the apex of a typical GNE used in the experiment with an apex radius of about 100 nm. After insulation, the typical exposed surface area of the apex is in the range of 1-4 μ m², as derived from the steady-state CVs (see Figure S1). The scheme in Figure 1c illustrates a typical hit-n-run collision event of a negatively charged 40 nm GNP on the SAM-covered GNE apex, which leads to the transient formation of a plasmonic metal-molecule-metal junction.²⁷

Figures 1d (i) to (iii) are the schematic illustrations of three different surface functionalizations we used on the GNE surface. The hydrophobic BPT molecule is a widely used Raman reporter molecule. The zwitterionic molecule CBT and PEG molecule are neutral and hydrophilic, which are often used to form a 'stealth' surface on nanoparticles for biomedical applications. To form mixed SAM surfaces, the BPT is mixed with either CBT or PEG. The BPT and CBT have similar molecular lengths. In contrast, the PEG-5k has an approximate contour length of 31.8 nm. ³⁴ However, when modified on the surface, the PEG molecules normally take different configurations ³⁴ depending on the total surface area available for modification and the surrounding environment. After mixing with the hydrophobic BPT molecules, we expect the PEG molecules to form the "mushroom" configurations on the GNE surface with a Flory radius (R_F) of about 4.8 nm. ³⁴

OCP Changes of Nanoelectrodes Induced by GNP Collision Events. We first discuss the results of the potentiometric measurement of bare GNEs. Before adding the 40 nm GNPs in the bath solution, no potential changes were observed in the potential-time (Vt) trace (see section S8, Supplemental Material). In a few minutes after adding GNPs to the bath solution at 50 pM of concentration, distinct and transient potential dips were observed (see the first V-t trace in Figure 2a). These potential dips are very similar to the ones induced by the collision of individual GNPs on the surface of CNE¹⁵ (see Supplemental Material S1 for CNE fabrication details). This suggests that these are due to the collision events of individual GNPs on the GNE apex and are governed primarily by the charge sensing model. In each collision event, the negatively charged GNP transiently lowers the surface potential of the floating GNE. Since no external forces such as electrical bias are applied to the GNE, the motion of the GNPs in the solution is mainly due to diffusion. Likely due to the hindered diffusion near the GNE apex³⁵ and dynamic interactions with the GNE surface, 28 the collision rate is not always constant but often increased gradually to reach a maximum. Afterward, it is reduced, which is attributed to the permanent non-specific adsorptions of GNPs on the apex. These adsorbed GNPs not only occupy the space on GNE surface but also repel the newly approaching GNPs and prevent them come closer to the apex. The adsorbed GNPs are also often gradually form clusters on the surface. When these happen, the collision-induced transient potential dips disappear from the V-t trace. For the bare GNEs, this normally happens in a few minutes, which is much shorter than the case of CNE.

To better understand these hit-n-run collision events, we divided a recorded potential dip from one collision event into two sections with time points t_1 , t_2 , and t_3 , as highlighted in the first trace of Figure 2a. To further understand the motion of GNPs during the collision, the dV/dt time traces (black) are also plotted below each V-t trace. The magnitude of dV/dt is a relative measure of the speed of GNPs during the collision. At time t₁, the GNP begins to approach the GNE apex and enters the potential sensing zone. It moves fast at the beginning, as evidenced by the obvious negative peak in the corresponding dV/dt time trace. When it moves very close to the GNE surface, it slows down and roams near the surface for a while. During this time, the potential change is small and the magnitude of dV/dt is very close to zero. At time t_2 , the potential suddenly increases, indicating the rebounding of the GNP from the GNE surface. Correspondingly, a large positive peak appears in the dV/dt time trace at t_2 . At time t3, the potential almost restores to its initial level of time t1. Another event happens immediately. For all these transient signals, the approach time duration ΔT_a $(=t_2-t_1)$ is very long while the rebound time duration $\Delta T_r (=t_3-t_2)$ is short. The difference between the two potentials at $t=t_2$ and $t=t_3$ is defined as ΔV . The magnitude of ΔV depends on the distance (D) between GNP and GNE surface during the hit-n-run collision event (also see Figure 5d). The ΔV is bigger when the GNP can approach closer to the GNE surface during the collision event.

To understand how the surface chemistry affects the potential changes, we conducted the nano-impact potentiometric measurements with CNE and BPT functionalized GNE. The results are also shown in Figure 2a (for additional data, see section S7, Supplemental Material). Compared with the bare GNE, the potential dips continued to appear for a much longer time with CNE. A similar phenomenon was observed for BPT GNE. In addition, the BPT GNEs, in general, produced more frequent potential dips among these three types of NEs. This happens because the BPT SAM makes the GNE surface highly hydrophobic, effectively reducing the chances of the negatively charged GNPs getting closer and attaching to the surface (see the SEM image in Figure S1e).

In addition, the shape of the potential dips is different with different NEs. Compared with bare GNE, the potential dips from CNE are more in the sawtooth shape. This suggests the GNPs have a uniform approach speed towards the CNE surface. The GNPs also rebound immediately after reaching the closest point, without roaming near the GNE surface. After introducing a BPT SAM on the bare GNE surface, the ΔV and the total time duration of the potential dips become smaller and shorter, respectively. The shape of the dips from BPT GNEs is closer to the ones from CNEs. We further conducted a statistical analysis of ΔV and ΔT_a of these dips happening on three different surfaces with comparable surface areas. As shown in Figures 2b and 2c, among the three, the ΔV and ΔT_a are the biggest for the bare GNE and smallest for the BPT GNE. This means that GNPs do not like to get closer to the BPT functionalized surface and spend less time in the vicinity of the surface during the collision. The results demonstrate the surface properties of NEs strongly affect the potential signals of nano-

OCP Changes of GNEs Modified with Mixed SAM of BPT/PEG and BPT/CBT.

The results in Figure 2 suggest the bare GNE is prone to non-specific adhesion, preventing reliable long-term measurements. The BPT modified GNE can effectively reduce GNP adsorption to enable continuous measurements of hit-n-run collision events. However, as revealed by the reduced ΔV magnitude of potential dips, the BPT monolayer is very hydrophobic and hinders the charged GNPs to approach closer to the GNE surface. This would also make the simultaneous SERS detection less probable (see the next section). To reduce the hydrophobicity of the BPT modified GNE surface, we formed mixed SAM by introducing hydrophilic molecules PEG or CBT in the BPT SAM. The GNEs modified with mixed SAM were investigated by CVs (see Figure S1). They could still effectively suppress the faradaic current, suggesting excellent surface coverages. Interestingly, the faradaic currents did not recover after GNP adsorptions. This phenomenon is different from the GNEs modified with conductive molecules such as 4-aminothiophenol or short alkane-dithiol.²⁷ The limited faradaic currents also suggest the amperometry approach cannot be used for BPT/PEG and BPT/CBT modified GNEs. As we will show below, the potentiometric method is still suitable for these highly resistive surface modifications, which is due to the longer sensing range of the potentiometric method.

Figure 3a shows the typical V-t and the corresponding dV/dt time traces containing GNP collision-induced transient potential signals (see section S7, Supplemental Material). The shape of these potential dips is greatly impacted by the surface functionalization of GNE. For BPT GNEs, the potential dips are generally uniform in their shapes (see Figure 2a). Here, after mixing with CBT or PEG, the potential signals become non-uniform (see Figure 3a), which may be attributed to the increased surface inhomogeneity. In general, the ΔV and ΔT_a of the potential dips from GNEs with BPT/CBT and BPT/PEG mixed SAM are much bigger than the ones from BPT GNEs. The trends are also clearly displayed in the statistical analysis of ΔV and ΔT_a in Figures 3b and 3c respectively. This happens because the hydrophobicity of the mixed SAM surface is reduced, allowing the GNPs to get closer to and stay longer near the GNE surface. Also, as compared to the ones from BPT/CBT GNEs, the distributions of ΔV and ΔT_a are much broader with a bigger mean value for BPT/PEG GNEs. Also, the rebounding time ΔT_r (a blue highlighted region in Figure 3a) of the colliding GNPs on the BPT/PEG GNE surface is significantly increased. These differences suggest the introduction of PEG to the BPT monolayer also introduce stronger GNP-surface interactions. The stronger interactions can be attributed to the more complex surface structure of the BPT/PEG SAM on the GNE surface, as illustrated in the schematics of Figure 1d (iii). This in turn would lead to increased non-specific adsorption of GNPs on the surface. This is also clearly demonstrated in SEM images which show significantly more GNPs attaching to the apex of BPT/PEG GNE (Figure S1e), as compared to the BPT/CBT GNE (Figure 1b). These results lead to a conclusion that the BPT/CBT GNE surface is not only hydrophilic enough to allow GNPs to get closer but also stealth enough to shield the surface from non-specific GNP adsorptions.

Transient SERS Signals of GNP Collision Events on the BPT Modified GNEs. We further studied the SERS signals induced by the GNP collisions. Before adding GNPs in the 10 mM PBS bath solution, no SERS signal of the Raman reporter molecule BPT was observed (see section S8, Supplemental Material). This is because the electrochemically etched GNE surface is quite smooth and thus not an effective SERS substrate, providing a clean SERS background to study individual GNP collision events. After adding 40 nm GNPs at 50 pM concentration in the bath solution, the SERS signals of BPT began to rise. The increase of the SERS signal is due to the gradual adsorption of GNPs on the GNE surface. Meanwhile, transient SERS bursts occur from time to time. These transient SERS intensity changes are signatures of GNP hit-n-run collision events on the GNE apex. 27, 29, 33, 36 The approaching of the GNP to the GNE surface leads to the transient formation of a new SERS hot spot in the GNP-on-GNE structure, resulting in the transient boost of BPT Raman signal. Figure 4a shows a typical SERS trajectory in a heatmap containing an individual GNP collision event as indicated by a transient intensity enhancement (enclosed by the dashed yellow lines). The bottom panel of Figure 4a shows the time-averaged SERS spectrum (black) of the trajectory, which reflects the stable background of the trajectory. The averaged SERS spectrum is very close to the DFT-calculated spectrum (red) based on the BPT-Au5 cluster complex (see section S4, Supplemental Material). To make the notations simpler, the major peaks at 1080 cm⁻¹ (coupled ring mode of BPT) and 1585 cm⁻¹ (C-H rocking mode of BPT) are referred to as modes v1 and v2, respectively.³⁷ We also replotted the time-resolved intensity changes of modes v1 and v2 in Figure 4b. The transient intensity increase is indicated as ΔI_{v1} for mode v1 and ΔI_{v2} for mode v2, which are obvious in the intensitytime (I-t) traces.

We also conducted SERS measurements for BPT/PEG and BPT/CBT GNEs. Compared with BPT, the Raman scattering cross-sections of both PEG and CBT are negligibly small. Therefore they do not contribute any interference Raman peaks to the BPT peaks under our SERS measurement conditions (see section S6, Supplemental Material). To understand the effect of surface chemistry on the GNP collisions, we monitored the I_{v2} of BPT from GNEs with different surface functionalization (see Figure 4c) for over 30 minutes right after adding the GNPs in the bath solutions. Different from the *I-t* trace in Figure 4b where the time resolution is 50 ms, each point in Figure 4c is the average of 1-minute data. The intensity of mode v2 (the SERS intensity baseline) depends on the number of GNPs adsorbed (permanent hot spots) on the GNE surface.

The dynamic changes in I_{v2} strongly depend on surface functionalization. For the BPT GNE, the I_{v2} increases gradually and reaches approximately 200 counts after 30 minutes. However, for the BPT/PEG GNE, I_{v2} increases fast to about 500 counts in the first 7-8 minutes and the overall intensity reaches 900 counts in 30 minutes, suggesting significantly more GNPs permanently attached to the GNE surface. This difference in the extent of GNP adsorptions can also be seen in the SEM images of Figure S1, as we discussed previously. In contrast, for the BPT/CBT GNE, the I_{v2} grows to approximately 300 counts in the first 10 minutes and then drops down to around 100

counts at the end of 30 minutes. Therefore, the BPT/CBT surface prevents the GNPs to stay permanently on the GNE surface and keeps the GNE apex clean to keep attracting new GNPs. This is also consistent with the SEM image in Figure 1b.

We further compared the intensity changes of I_{v2} . We examined a short time trace of 50 s duration (with 50 ms time resolution) near 8 minutes in Figure 4b by plotting the first derivative of I_{v2} (dI_{v2} /dt). As shown in (i) of Figure 4c, the largest fluctuations in dI_{v2} /dt appear for BPT/CBT GNE, which are induced by the frequent occurrence of the hit-n-run type of collision events and the longer duration time of each collision event. In contrast, the fluctuations are much smaller for the BPT/PEG and BPT GNEs. For the BPT/PEG GNE, the big fluctuations are only observed in the first few minutes. At 8 minutes, a lot of GNPs already attached to the GNE surface, preventing new collision events.

Thus, compared with BPT and BPT/PEG GNEs, the BPT/CBT GNE is ideal for long-time GNP nano-impact measurements using both OCP and SERS methods for two reasons. Firstly, the BPT/CBT modification protects the GNE surface from non-specific adsorption of GNPs. Secondly, it allows the GNPs to stay closer to the GNE surface, generating bigger potential and SERS intensity changes and enhancing detection sensitivity. In contrast, the increased non-specific adsorptions of GNPs trigger aggregations on the GNE surface, prevent continuous uniform 'hit-n-run' events and generate huge SERS background. Therefore, we mainly used the BPT/CBT GNEs for the simultaneous SERS and OCP measurements.

Simultaneous OCP and SERS Detection of GNP Collision Events on BPT/CBT Modified GNEs. After optimizing the surface modification conditions for detecting continuous GNP hit-n-run collision signals, simultaneous OCP and SERS measurements were conducted by using BPT/CBT GNEs. Figure 5a shows the representative result of a GNP collision-induced transient SERS intensity changes (top panel) and the corresponding potential changes (pink curve, bottom panel). As a reference, I_{v2} -t (olive) trace is also plotted in the bottom panel. The potential begins to fall long before the appearance of detectable changes in the SERS trajectory. The potential drop suggests the GNP enters the potential detection zone of the GNE. Once it drops close to the lowest point, indicating that the GNP is very close to the GNE surface, the SERS intensity bursts often suddenly appear.

Figure 5b shows another example with both V-t (pink) and I_{v2} -t (olive) traces. The dV/dt time trace (blue) is also plotted to better understand the GNP motion during the collision. The distinct dV/dt spikes are due to the fast rebound of the colliding GNPs from the BPT/CBT GNE surface. Three collision events (E₁ to E₃) are obvious in the dV/dt time trace. Among the three events, only the potential dip of E₂ is accompanied by a transient above noise level increase in I_{v2} . However, the remaining two events detected as potential changes did not trigger above noise level changes in I_{v2} . For most of the correlated events such as E₂, the transient SERS intensity changes were triggered before the rebounding of GNP. Therefore, the colliding GNPs are expected to spend time moving in random motion very close to the BPT/CBT GNE surface before rebounding away because the light field enhancement in the gap mode is very sensitive

to the gap distance. This is consistent with our analysis of GNP collision dynamics based on the shape of potential dips in potentiometric measurements.

We further conducted a statistical analysis of 50 collision events of E_2 type with simultaneous changes in ΔV and ΔI_{v2} . Figure 5c shows the scatter plot between the ΔV and ΔI_{v2} . The solid line is the linear regression fit. The Pearson's correlation coefficient r obtained from the fit is 0.43, suggesting a moderate correlation. A similar correlation can be seen between ΔV and ΔI_{v1} (see section S8, Supplemental Material). In general, the bigger ΔV s are often coupled with the bigger ΔI s.

The overall poor correlation between the collision induced potential and SERS signals could be attributed to two reasons: (i) the collision events detected in the potential measurement did not happen inside the detection cross-section of the objective lens used in SERS measurement; (ii) the GNPs did not approach closely enough to the GNE surface to induce detectable SERS intensity changes. For the first reason, the collision-induced SERS intensity changes can only be collected from a limited surface area of the GNE apex facing the objective lens (see Figure 1a), whereas, the changes in ΔV can be induced by the GNP collision events that happen on the entire surface of the exposed GNE apex. We will further discuss the second reason below.

To better understand the GNP-GNE distance (D) dependence of ΔI and ΔV , we carried out FDTD and FEM simulations, respectively. The details of FDTD simulation on the light field enhancement inside the GNP-GNE nanogap are given in section S3 of Supplemental Material. The GNP-on-GNE structure is similar to the intensively studied structure of GNP on the gold thin film, which is the so-called NP-on-mirror structure. 38 As shown in Figure S3, the GNP on the GNE is highly effective to focus light down to the tiny volume containing a small number of BPT molecules in the nanogap under the GNP. The light field enhancement in the nanogap is also extremely sensitive to the gap distance D, which can modulate the coupling of plasmon resonance of two neighboring gold structures.^{25, 39, 40} In the FDTD simulation, the ΔI is proportional to the fourth power of the electric field enhancement (|E/E₀|⁴), where E is the local electric field at the center of BPT SAM (thickness 1.3 nm) in the nanogap between GNP and GNE and E₀ is the electric field of the incident laser. The details for the FEM simulation of the GNP induced potential change on the floating GNE are given in section S5 of Supplemental Material. The potential changes of a floating GNE is simulated when a nearby GNP is placed at Ds. Results of FDTD and FEM simulations are shown in Figure 5d. We used $|E/E_0|^4$ to represent the ΔI . The $|E/E_0|^4$ drops much faster than the ΔV over the same D. The solid lines are the exponential decay fittings $(y = ae^{-bx})$ for both $|E/E_0|^4$ and ΔV . The decay constant of the $|E/E_0|^4$ -D curve is more than 10 times bigger than that of ΔV -D curve. Therefore, the potential sensing zone is much bigger than the SERS sensing zone. This can also explain why we observe the potential changes much earlier or do not observe the corresponding SERS intensity changes at all during some of the collision events. One way to further improve the correlation is to further optimize the surface modification to better regulate GNP-GNE distance during the collision, helping generate uniform and continuous 'hit-n-run' events while preventing the occurrence of 'hit-n-stay' events.

Conclusions

In summary, we have successfully extended the potentiometric nano-impact method from CNE to GNE. One of the main problems associated with the bare GNE is the non-specific adhesion of the analytes making it ineffective for long-term measurements. To solve this problem, we have functionalized the GNE apex surface with different surface properties. Compared with CNE, the facile surface chemistry on GNE provides new opportunities for us to explore how the surface chemistry affects the collision dynamics of nano entities. In addition, the GNE is an excellent plasmonic substrate. We have probed individual GNP collision events on surface functionalized GNEs using both the potentiometric and SERS methods. The hydrophobic BPT SAM prevented the GNPs to get closer to the GNE surface and reduced the magnitude of the potential changes. By mixing BPT with hydrophilic CBT, the potential changes are enhanced while still effectively preventing non-specific GNP adsorptions. Compared with CBT, stronger interactions are found between PEG and GNPs, leading to significant non-specific GNP adsorptions at the GNE apex. By using BPT/CBT modification, we achieved continuous recording of GNP collision events through timeresolved OCP and SERS measurements. The simultaneously measured transient potential and SERS changes helped us to better understand the GNP collision dynamics and the GNP-surface interactions. However, we only found a moderate correlation between the simultaneously measured potential and SERS changes. The FDTD and FEM simulations revealed the very different distance-dependent relationships between potential and SERS intensity.

The facile GNE based potentiometric nano-impact method has the potential to work as a low-cost label-free technique to detect various charged nanoscale entities. To enable practical applications for reliable single-molecule detection of biomolecules such as protein, DNA, and RNA, the proper functionalization of the GNE surface is important to improve the reliability, sensitivity, and specificity of this method when working in a complex medium. This work provides insight into the development of effective surface functionalization strategies. By capturing analytes to the GNP surface, we can also detect the analytes based on their molecular fingerprints in Raman spectroscopy and study the dynamic molecular recognition process in the nanogap of GNP-GNE using the simultaneous potential and SERS measurements reported in this work.

Acknowledgments

This work was supported by NSF CBET 1454544 and CHE 2003785. We thank FIU AMERI for the use of the SEM facility. The author thanks Mr. Jianghao Zhou for his help in DFT calculations.

ORCID

Jin He: https://orcid.org/0000-0002-2633-9809

Joongho Moon: https://orcid.org/0000-0001-6178-4628

Jing Guo: https://orcid.org/0000-0001-7292-6265

Golam Sabbir Sarker: https://orcid.org/0000-0003-0518-5940

REFERENCES

- 1. W. Wang and N. Tao, Anal. Chem., 86, 2 (2014).
- 2. Y. Wang, X. Shan and N. Tao, Faraday Discuss., 193, 9 (2016).
- 3. R. M. Crooks, *Faraday Discussions*, **193**, 533 (2016).
- 4. L. A. Baker, J. Am. Chem. Soc., 140, 15549 (2018).
- 5. S.-M. Lu, Y.-Y. Peng, Y.-L. Ying and Y.-T. Long, *Anal. Chem.*, **92**, 5621 (2020).
- 6. K. Fu, S.-R. Kwon, D. Han and P. W. Bohn, Accounts of Chemical Research, 53, 719 (2020).
- 7. H. Ren and M. A. Edwards, Current Opinion in Electrochemistry, 25, 100632 (2021).
- 8. B. M. Quinn, P. G. van't Hof and S. G. Lemay, *J. Am. Chem. Soc.*, **126**, 8360 (2004).
- 9. X. Xiao and A. J. Bard, J. Am. Chem. Soc., 129, 9610 (2007).
- 10. X. Xiao, F.-R. F. Fan, J. Zhou and A. J. Bard, J. Am. Chem. Soc., 130, 16669 (2008).
- 11. J. Kim, B.-K. Kim, S. K. Cho and A. J. Bard, *J. Am. Chem. Soc.*, **136**, 8173 (2014).
- 12. J. E. Dick, C. Renault and A. J. Bard, J. Am. Chem. Soc., 137, 8376 (2015).
- 13. T. J. Anderson and B. Zhang, Acc Chem Res, 49, 2625 (2016).
- 14. H. Zhou, J. H. Park, F.-R. F. Fan and A. J. Bard, J. Am. Chem. Soc., 134, 13212 (2012).
- 15. P. Pandey, J. Garcia, J. Guo, X. Wang, D. Yang and J. He, *Nanotechnology*, **31**, 015503 (2019).
- 16. P. Pandey, G. Ghimire, J. Garcia, A. Rubfiaro, X. Wang, A. Tomitaka, M. Nair, A. Kaushik and J. He, *ACS Sensors*, **6**, 340 (2021).
- 17. N. Panday, G. Qian, X. Wang, S. Chang, P. Pandey and J. He, ACS Nano, 10, 11237 (2016).
- 18. P. Pandey, N. Bhattarai, L. J. Su, X. W. Wang, F. F. Leng, B. Gerstman, P. P. Chapagain and J. He, *Acs Sensors*, **Accepted** (2022).
- 19. E. Zdrachek and E. Bakker, Anal. Chem., 91, 2 (2019).
- 20. J. Greenwood, T. H. Phan, Y. Fujita, Z. Li, O. Ivasenko, W. Vanderlinden, H. Van Gorp, W. Frederickx, G. Lu, K. Tahara, Y. Tobe, H. Uji-i, S. F. L. Mertens and S. De Feyter, *ACS Nano*, **9**, 5520 (2015).
- 21. M. C. Rodríguez González, A. Brown, S. Eyley, W. Thielemans, K. S. Mali and S. De Feyter, *Nanoscale*, **12**, 18782 (2020).
- 22. A. Ulman, *Chemical Reviews*, **96**, 1533 (1996).
- 23. J. Guo, X. Yan, M. Xu, G. Ghimire, X. Pan and J. He, Anal Chem, 93, 4441 (2021).
- 24. I. Tokareva, S. Minko, J. H. Fendler and E. Hutter, J. Am. Chem. Soc., 126, 15950 (2004).
- 25. R. T. Hill, J. J. Mock, Y. Urzhumov, D. S. Sebba, S. J. Oldenburg, S.-Y. Chen, A. A. Lazarides, A. Chilkoti and D. R. Smith, *Nano Lett.*, **10**, 4150 (2010).
- 26. C.-H. Chen, E. R. Ravenhill, D. Momotenko, Y.-R. Kim, S. C. S. Lai and P. R. Unwin, *Langmuir*, **31**, 11932 (2015).
- 27. J. Guo, J. Pan, S. Chang, X. Wang, N. Kong, W. Yang and J. He, Small, 14, 1704164 (2018).
- 28. H. Ma, J.-F. Chen, H.-F. Wang, P.-J. Hu, W. Ma and Y.-T. Long, *Nature Communications*, **11**, 2307 (2020).
- 29. N. Kong, J. Guo, S. Chang, J. Pan, J. Wang, J. Zhou, J. Liu, H. Zhou, F. M. Pfeffer, J. Liu, C. J.

- Barrow, J. He and W. Yang, *J. Am. Chem. Soc.*, **143**, 9781 (2021).
- 30. S. Schöttler, G. Becker, S. Winzen, T. Steinbach, K. Mohr, K. Landfester, V. Mailänder and F. R. Wurm, *Nature Nanotechnology*, **11**, 372 (2016).
- 31. J. B. Schlenoff, *Langmuir*, **30**, 9625 (2014).
- 32. F. Sun, J.-R. Ella-Menye, D. D. Galvan, T. Bai, H.-C. Hung, Y.-N. Chou, P. Zhang, S. Jiang and Q. Yu, *ACS Nano*, **9**, 2668 (2015).
- 33. Q. Ai, J. Zhou, J. Guo, P. Pandey, S. Liu, Q. Fu, Y. Liu, C. Deng, S. Chang, F. Liang and J. He, *Nanoscale*, **12**, 17103 (2020).
- 34. C. Cruje and D. B. Chithrani, Reviews in Nanoscience and Nanotechnology, 3, 20 (2014).
- 35. E. Kätelhön and R. G. Compton, *Chemical Science*, **5**, 4592 (2014).
- 36. T. Ma, J. Guo, S. Chang, X. Wang, J. Zhou, F. Liang and J. He, *Phys Chem Chem Phys*, **21**, 15940 (2019).
- 37. F. Benz, C. Tserkezis, L. O. Herrmann, B. de Nijs, A. Sanders, D. O. Sigle, L. Pukenas, S. D. Evans, J. Aizpurua and J. J. Baumberg, *Nano Lett.*, **15**, 669 (2015).
- 38. P. K. Aravind, R. W. Rendell and H. Metiu, *Chemical Physics Letters*, **85**, 396 (1982).
- 39. J. J. Mock, R. T. Hill, A. Degiron, S. Zauscher, A. Chilkoti and D. R. Smith, *Nano Lett.*, **8**, 2245 (2008).
- 40. G. Lévêque and O. J. F. Martin, Opt. Express, 14, 9971 (2006).

FIGURES:

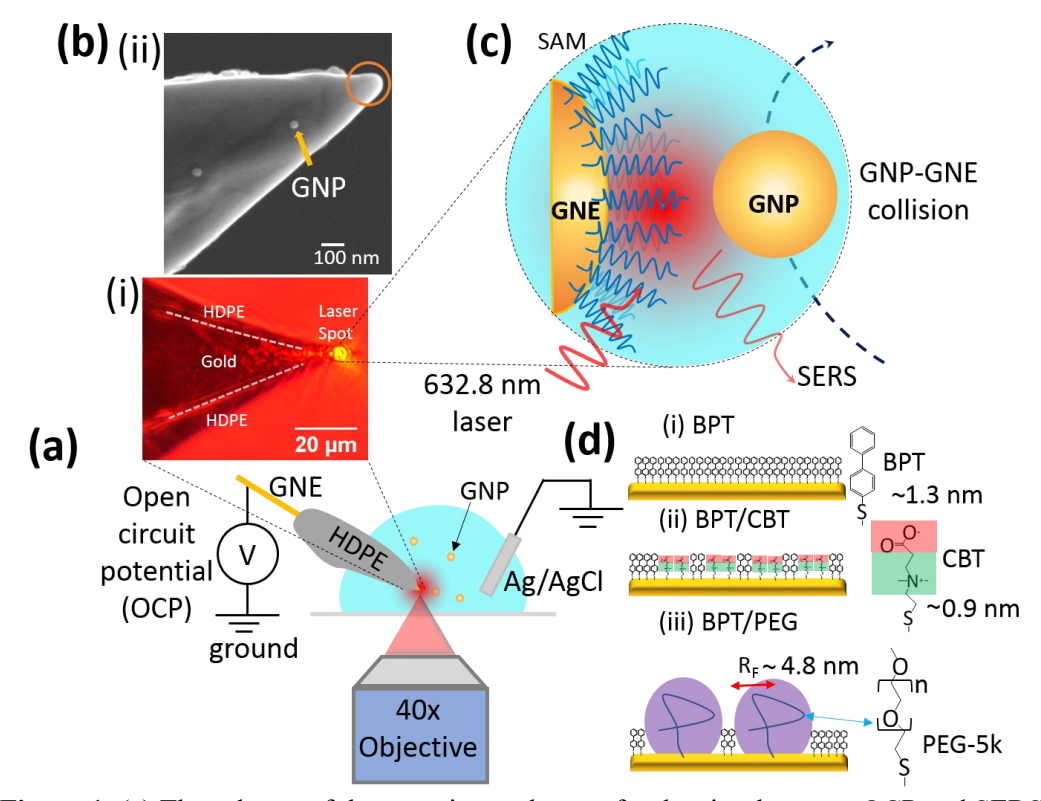


Figure 1: (a) The scheme of the experimental setup for the simultaneous OCP and SERS measurements of GNP collision events on a GNE apex. The bath solution (10 mM PBS) is grounded with a quasi-reference Ag/AgCl electrode. (b) (i) An optical microscope image of a HDPE insulated GNE irradiated by a focused laser beam during the actual experiment. The dashed white lines mark an approximate boundary of gold and HDPE. (ii) SEM image of a BPT/CBT modified GNE after exposing to GNPs solution. The yellow arrow marks an adsorbed 40 nm GNP. To achieve better image quality, the GNE used in SEM imaging is not insulated. The orange circle shows the region of GNE apex which would typically be exposed after the HDPE insulation. (c) An enlarged schematic illustration of the collision event of a GNP on the GNE surface modified by a SAM. (d) Schematic illustration of GNE surfaces with three types of SAM: (i) BPT, (ii) Mixed BPT/CBT and (iii) Mixed BPT/PEG. The molecular structures and their approximate lengths are also shown.

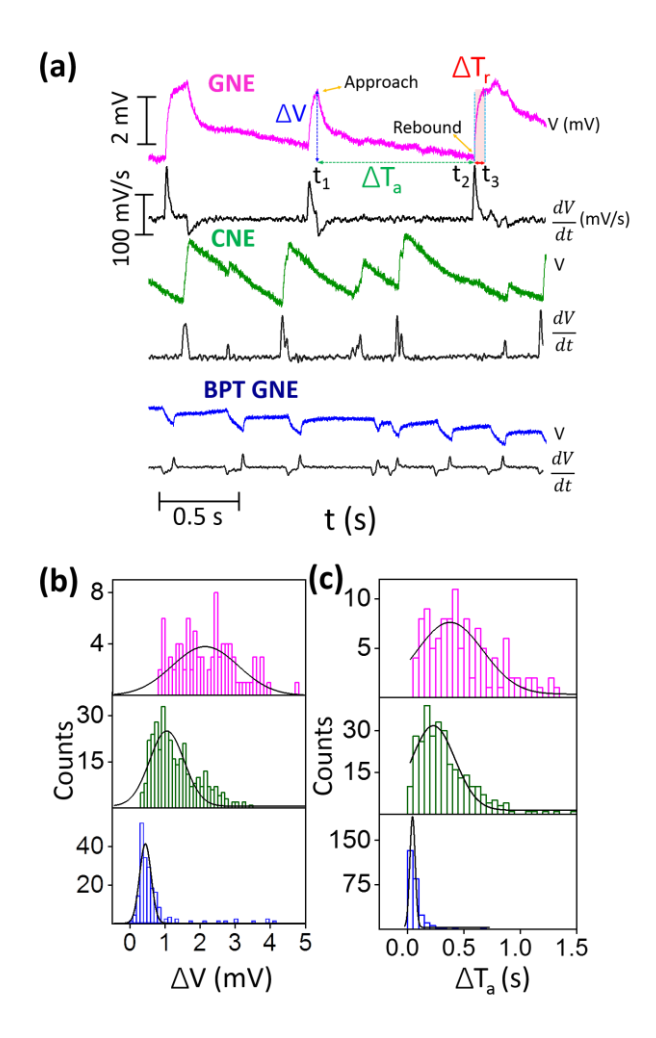


Figure 2: Comparison of OCP amplitudes (ΔV) and approach time durations ($\Delta T_a = t_2 - t_1$) of GNE (N=127), CNE (N=200) and BPT GNE (N=190). (a) Typically observed *V-t* traces with GNE (pink), CNE (green) and BPT GNE (blue). The dV/dt time traces (black) are plotted below each *V-t* trace. The red shaded region denotes the rebound time duration $\Delta T_r = t_3 - t_2$. (b) The ΔV histograms of GNE (pink) with mean 2.14 ± 0.94 mV, CNE (green) with mean 1.15± 0.49 mV, and BPT GNE (blue) with mean 0.4 ± 0.16 mV. (c) The ΔT_a histograms of GNE (pink) with mean 377.7±26.3 ms, CNE (green) with mean 230.9±82.3 ms, and BPT GNE (blue) with mean 45.0 ±11.2 ms. The solid black lines are the Gaussian fits.

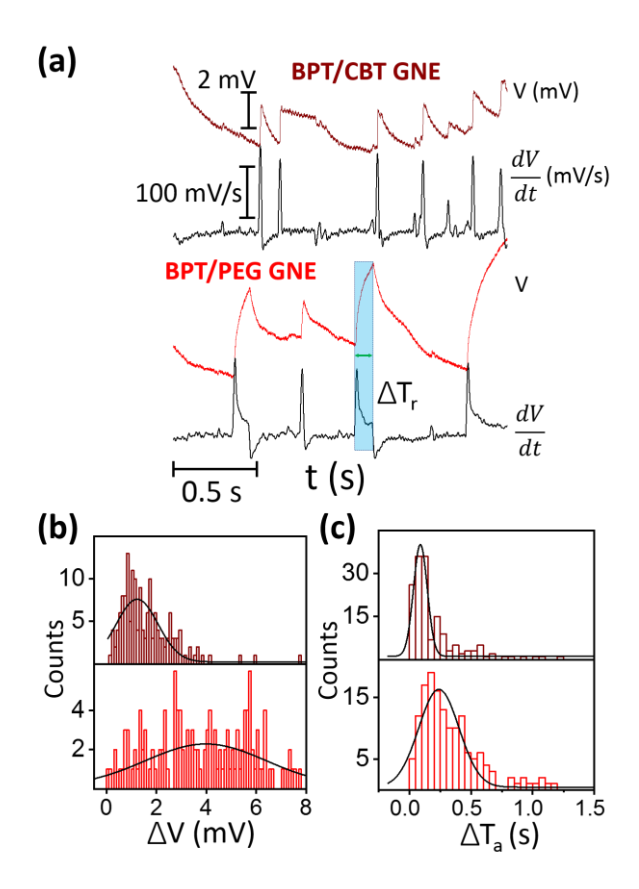


Figure 3: Comparison of OCP amplitudes and approach time durations of GNE with BPT/CBT (N=162), and BPT/PEG (N=160). (a) Typically observed V-t traces for GNEs with BPT/CBT (maroon) and BPT/PEG (red). The dV/dt time traces (black) are plotted below each V-t trace. The blue shaded region denotes the rebound time duration ΔT_r . (b) ΔV histograms for GNEs with BPT/CBT (maroon) with mean 1.22 ± 0.83 mV and BPT/PEG (red) with mean 4.90 ± 1.42 mV. (c) ΔT_a histograms for BPT/CBT GNEs with mean 88.9 ± 45.1 ms and for BPT/PEG GNEs with mean 238.8 ± 80.5 ms. The solid black lines are the Gaussian fits.

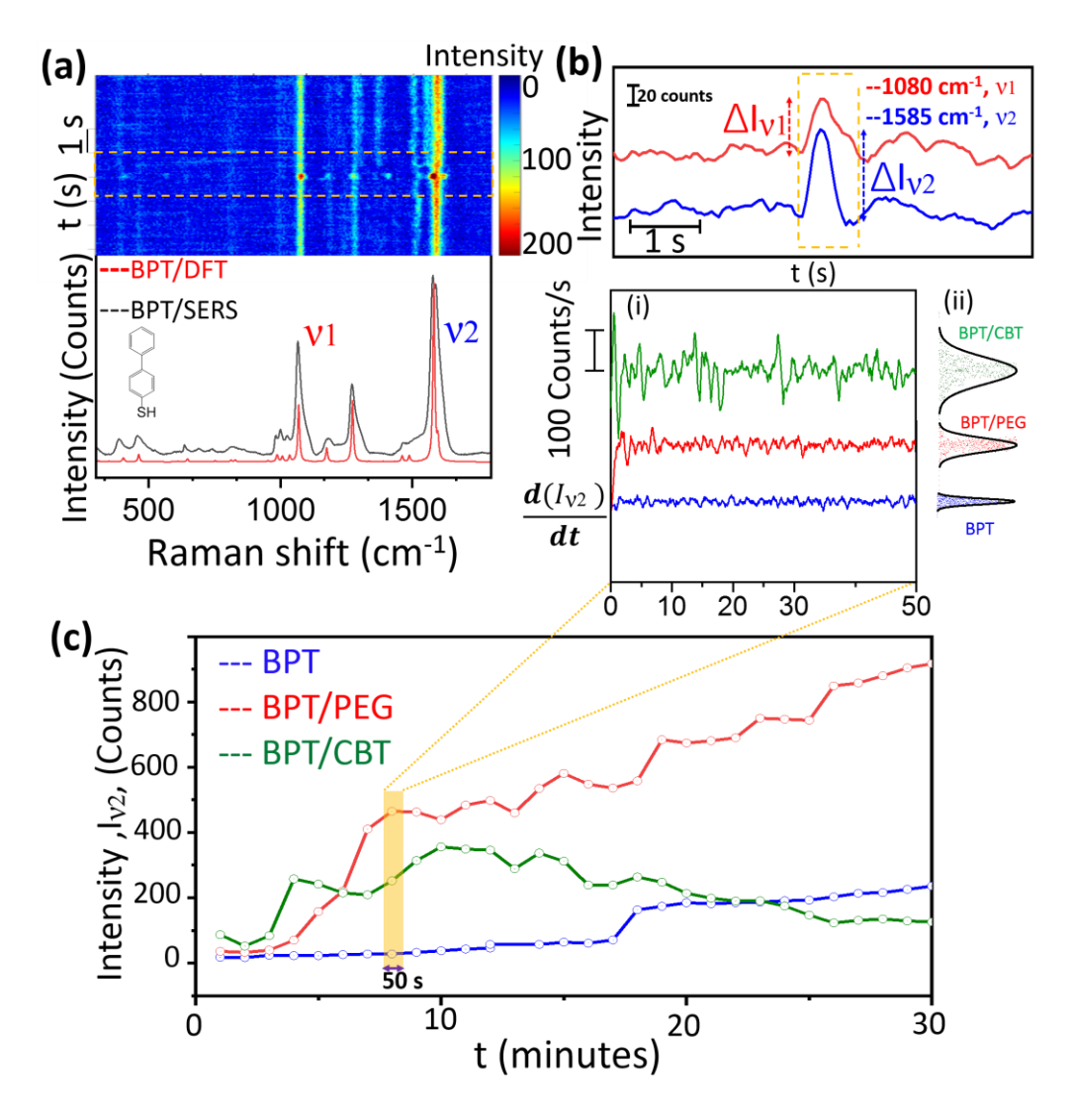


Figure 4: (a) SERS intensity heatmap showing single hit-n-run event detected as a transient SERS intensity increase (top), SERS spectra, and DFT calculated spectra of BPT molecule (bottom). (b) SERS intensity-time traces for two major peaks 1080 cm⁻¹ (v1) and 1585 cm⁻¹ (v2) of BPT, which contains a hit-n-run event. (c) The I_{v2} -t traces (averaged for 1 min) from GNEs functionalized with BPT (blue), BPT/PEG (red), and BPT/CBT (olive). The yellow highlighted section is enlarged showing (i) the dI_{v2}/dt time trace near 8 minutes and (ii) the magnitude distributions of dI_{v2}/dt . The solid lines are the Gaussian fits.

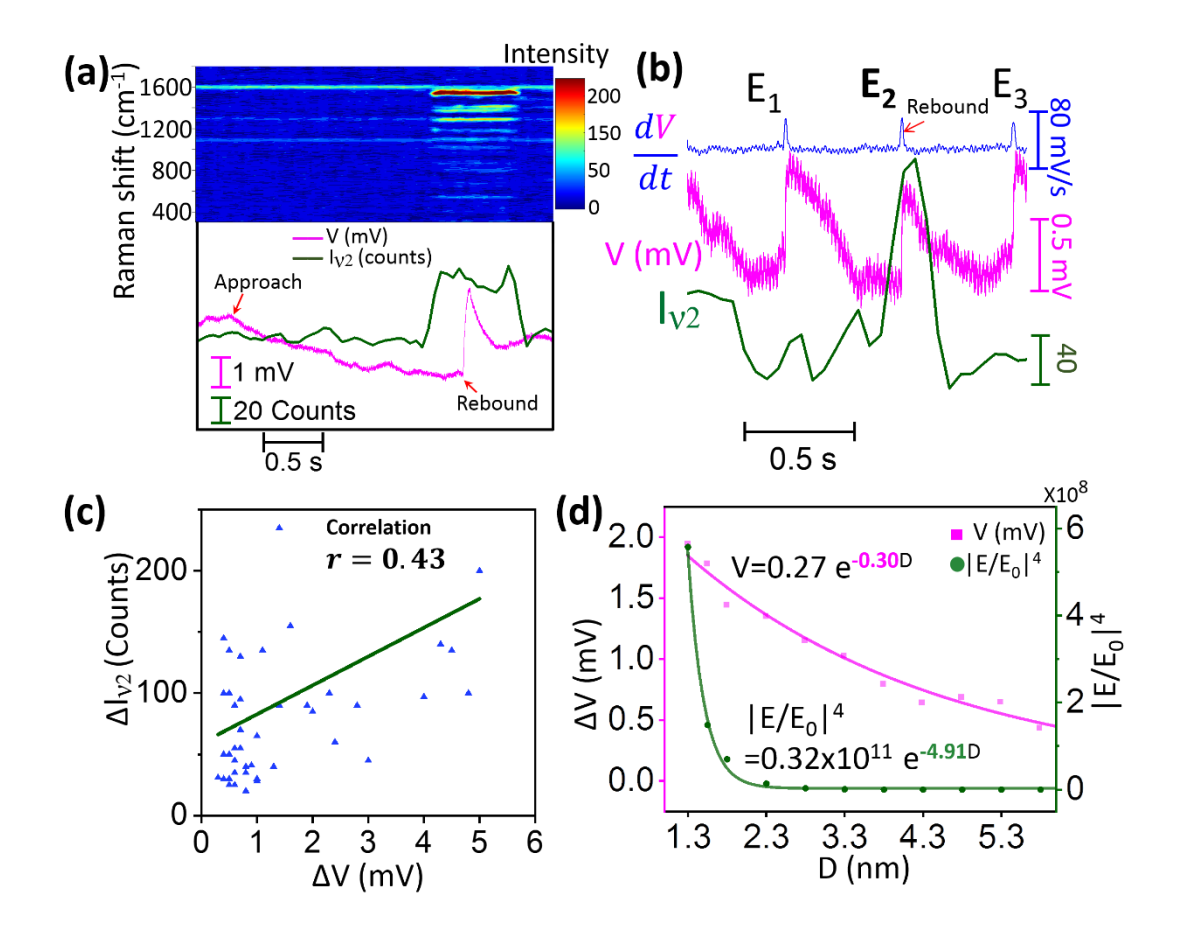


Figure 5: Simultaneous potential and SERS measurement of GNP collision events on the BPT/CBT GNE apex. (a) Top panel: The SERS trajectory in the heatmap of a typical hit-n-run type of collision event. Bottom panel: V-t (pink) and I_{v2} -t (olive) trace. (b) The V-t (pink) and I_{v2} -t (olive) traces with three (E₁ to E₃) collision events. The dV/dt time trace (blue) is also shown. (c) The ΔV vs. ΔI_{v2} scatter plot. The solid green line is the regression fit, resulting in Pearson's correlation r of 0.43. (d) The ΔV vs. D and $|E/E_0|^4$ vs. D plots from the FEM and FDTD simulations.